Acta Mechanica Sinica (2013) 29(3):399–410
DOI 10.1007/s10409-013-0028-z

RESEARCH PAPER

On aerodynamic noises radiated by the pantograph system of high-speed trains

Hua-Hua Yu · Jia-Chun Li · Hui-Qin Zhang

Received: 22 October 2012 / Revised: 6 February 2013 / Accepted: 12 March 2013

Abstract Pantograph system of high-speed trains become significant source of aerodynamic noise when travelling speed exceeds 300 km/h. In this paper, a hybrid method of non-linear acoustic solver (NLAS) and Ffowcs Williams–Hawkings (FW–H) acoustic analogy is used to predict the aerodynamic noise of pantograph system in this speed range. When the simulation method is validated by a benchmark problem of flows around a cylinder of finite span, we calculate the near flow field and far acoustic field surrounding the pantograph system. And then, the frequency spectra and acoustic attenuation with distance are analyzed, showing that the pantograph system noise is a typical broadband one with most acoustic power restricted in the medium-high frequency range from 200 Hz to 5 kHz. The aerodynamic noise of pantograph systems radiates outwards in the form of spherical waves in the far field. Analysis of the overall sound pressure level (OASPL) at different speeds exhibits that the acoustic power grows approximately as the 4th power of train speed. The comparison of noise reduction effects for four types of pantograph covers demonstrates that only case 1 can lessen the total noise by about 3 dB as baffles on both sides can shield sound wave in the spanwise direction. The covers produce additional aerodynamic noise themselves in the other three cases and lead to the rise of OASPLs.

Keywords Aerodynamic noise · NLAS · FW–H acoustic analogy · Pantograph system · High-speed train

The project was supported by the National Key Technology R&D Program (2009BAG12A03) and the Knowledge Innovation Project of Chinese Academy of Sciences of China (KJCX2-EW-L02-1).

H.-H. Yu · J.-C. Li (✉) · H.-Q. Zhang
LMFS, Institute of Mechanics,
Chinese Academy of Sciences,
100190 Beijing, China
e-mail: jcli05@imech.ac.cn

1 Introduction

With economic booming and urbanization speeding up, people have raised increasing demands on swift travel between two cities in the shortest time. The high-speed train as fast as 350 km/h seems to be a most attractive choice. Consequently, high-speed railway will be greatly developed in China in the next decade. On the other hand, attentions should be drawn to the issue of noise reduction of high-speed trains, a challenging problem in aerodynamics. The noise in the carriage may greatly influence the comfort of passengers while the noise radiated outward to ambient atmosphere may enormously disturb surrounding residents alongside the railway. As a result, the issue has become one of the major tasks during the design of high-speed trains.

Generally speaking, high-speed train noise comes from three kinds of sources, namely, noise of traction motor system, rolling noise and aerodynamic noise [1]. They play different roles in different train speed ranges. For traditional trains, the speed is very low and its noise comes mainly from traction motor system and rolling noise. Relevant research results [2] have shown that the traction motor system noise and rolling noise are respectively proportional to the first and third power of train speed. However, the acoustic power of aerodynamic noise grows as the 6th power of train speed. Consequently, with continuous increasing of train speed, the contribution of aerodynamic noise will eventually become the dominant factor. This critical speed generally falls within the range of 200 km/h to 300 km/h, different for different type of trains. Hence, it is necessary to study the genesis mechanism of aerodynamic noise of high-speed trains and propose corresponding measures.

Aerodynamic noise is generally caused by unsteady disturbances in the flow over uneven/rough surfaces or structural components of the train body, such as the train head, body surface, bogie areas, carriage gaps, pantograph system and compartment rear [3]. Relevant researches have demonstrated that the noise from pantograph system makes major

contribution to the total amount when the train speed exceeds 300 km/h. Therefore, it is requisite to make clear the genesis mechanism and propagation characteristics of pantograph noise.

In recent years, flow noise problem of high-speed trains has increasingly received researcher's attention. A great many experimental works have been carried out in wind tunnel tests. Noger et al. [4] investigated experimentally aeroacoustic features of TGV train pantograph recess on a 1:7 scale model both with and without pantographs in a low-speed acoustic wind tunnel. Takaishi et al. [5] compared the characteristics of flow fields and aerodynamic noises in the wake by testing three types of pantograph horn models, a simple cylinder, a cylinder with a continuous slit and a cylinder with periodic holes, in a low noise wind tunnel. Shibata et al. [6] developed a new type low noise pantograph by 1:5 and 1:10 scale model tests in an acoustic wind tunnel. Similarly, Nagakura [7] estimated the contribution of individual noise sources of Shinkansen trains to wayside noise level.

In addition, a lot of researchers have explored the countermeasures for noise reduction. Murata et al. [8] described the measures for the reduction of aerodynamic noises from current collecting system and the lower parts of Shinkansen trains. Kurita et al. [9, 10] developed two types of low-noise pantographs to lessen noise of the Shinkansen trains. Several sound-reduction devices on test train FASTECH360S, Z such as sound absorbing panels, pantograph noise insulation plates, and low noise pantograph were presented in Refs. [11, 12]. Based on sound source localization results of Shinkansen trains in wind tunnel test, Yamazaki et al. [13] proposed a few techniques to reduce the aerodynamic noise level arising from carriage gaps. Wakabayashi et al. [14] developed a high performance noise insulation panel, which itself is not a noise source. Sueki et al. [15] proposed a new aerodynamic noise reduction method by using a porous material cover, which was experimentally proved effective for a cylinder or pantograph. Ikeda et al. [16, 17] put forward a few noise reduction techniques, including the relief of aerodynamic disturbances between articulated frame and shape-optimized panhead.

As for numerical simulation, Talotte [18] gave a critical survey on computational studies on aerodynamic noises of high-speed trains. Holmes et al. [19] combined boundary element method (BEM) and finite element method (FEM) to calculate aerodynamic noise by a 1:10 scale model of pantograph cover at the speed of 250 km/h. Kitagawa and Nagakura [20] developed a method to calculate high-speed train noise and further analyzed the measured noise data on Shinkansen trains at 120 km/h or higher speed. Sassa et al. [21] carried out two-dimensional analyses of aerodynamic noises of a side door by FEM and BEM for incompressible fluid flow computation and for acoustic analysis, respectively. The flow field and aerodynamic noise of a power collection equipment were simulated by Yang et al. [22]. Masson et al. [23] carried out numerical simulations to study aerodynamic noise characteristics of the front part of a high-speed train at full scale based on lattice-Botzmann method (LBM). The results helped to identify primary noise sources and evaluate the geometrical optimizations.

These numeric methods were successfully applied to high-speed aeroacoustics analysis. However, previous studies focused mainly on train speeds lower than 350 km/h. As for the noise of important components of CRH train such as different types of pantograph systems at the speed of 350 km/h (flows with higher Reynolds number), the detailed information about noise genesis is still not clearly understood. In this paper, numerical method of a hybrid NLAS/FW–H acoustic analogy with penetrable integral control surface is used to study the characteristics of aerodynamic noises radiated by the pantograph system. The genesis mechanism of aerodynamic noises arising from pantograph systems is further discussed. The frequency spectra and acoustic attenuation characteristics are analyzed. Overall sound pressure levels (OASPLs) at standard observer point are calculated for different speed levels. Finally, four types of pantograph covers are compared to evaluate the effect of pantograph cover on aerodynamic noise radiation.

2 Numerical simulation methodology

Generally speaking, aerodynamic noise prediction can be performed directly or indirectly. The former solves both flow and acoustic fields based on direct numerical simulation (DNS) or large eddy simulation (LES), which needs large amount of computational resources due to tremendously high resolution requirement. Recently, Jiang Min et al. [24] conducted DNS of the flow around a NACA0018 airfoil and associated self-noise. Both the near-field hydrodynamics and the far-field acoustics were computed simultaneously. Hence, the latter known as hybrid method is preferred to solve the flow field nearby the body and the acoustic field far away by artificially separating the computational domain into the acoustic source and the acoustic propagation regions. Generally speaking, traditional computation al fluid dynamics (CFD) methods including DNS, LES/DES (detached eddy simulation) and Reynolds-averaged Navier–Stokes (RANS) equation methods are utilized for the near field while the linearized Euler equations (LEE) [25] method and acoustic analogy method [26] are employed for the far field.

In the present study, we adopt the hybrid method to analyze acoustic noise of the pantograph system of a high speed train. For the sake of further saving computational resources, we would rather use non-linear acoustic solver (NLAS) approach proposed by Paul Batten et al. [27] to obtain unsteady turbulent flows. Namely, we at first solve the Navier–Stokes (N–S) equation by using turbulent modeling and then calculate unsteady perturbations based on NLAS, which can achieve reasonable results with less number of grid cells, especially in the near-wall region, than DNS/LES does. In regard to the closure of RANS equations, a non-linear two-

equation cubic k-epsilon turbulence model [28] is employed in this paper so as to take into account more appropriately the anisotropic nature of the turbulence and the production of turbulent kinematic energy. Since the complicated solid surfaces are involved in the problem of pantograph system noise, FW–H formula as acoustic analogy [29] is used to estimate surrounding noise characteristics.

In summary, we need three steps to finally obtain the sound pressure level of a pantograph system at an arbitrary observer point in the far field. Firstly, steady RANS computation is performed to obtain an initial quasi-steady flow field for NLAS computation. Secondly, NLAS method is utilized to resolve near-field fluid flow and acoustic source. In this step, an penetrable integral control surface surrounding all the noise sources is set to store the unsteady flow information every time step. Finally, the far-field acoustic propagation is obtained by integrating FW–H equation over the penetrable integral control surface.

2.1 NLAS method

The governing equations of NLAS method proposed by Batten et al. [27] were derived from perturbations to the N–S equations, referred to as non-linear disturbance equations (NLDE)

$$\frac{\partial \boldsymbol{Q}'}{\partial t}+\frac{\partial \boldsymbol{F}_i'}{\partial x_i}-\frac{\partial (\boldsymbol{F}_i^{\nu})'}{\partial x_i}=-\frac{\partial \overline{\boldsymbol{Q}}}{\partial t}-\frac{\partial \overline{\boldsymbol{F}}_i}{\partial x_i}+\frac{\partial (\overline{\boldsymbol{F}}_i^{\nu})}{\partial x_i}, \tag{1}$$

where

$$\overline{\boldsymbol{Q}}=\begin{bmatrix}\overline{\rho}\\ \overline{\rho}\,\overline{u}_j\\ \overline{e}\end{bmatrix},\qquad \overline{\boldsymbol{F}}_i=\begin{bmatrix}\overline{\rho}\,\overline{u}_i\\ \overline{\rho}\,\overline{u}_i\overline{u}_j+\overline{p}\delta_{ij}\\ \overline{u}_i(\overline{e}+\overline{p})\end{bmatrix},$$

$$\overline{\boldsymbol{F}}_i^{\nu}=\begin{bmatrix}0\\ \overline{\tau}_{ij}\\ -\overline{\theta}_i+\overline{u}_k\overline{\tau}_{ij}\end{bmatrix},\qquad \boldsymbol{Q}'=\begin{bmatrix}\rho'\\ \overline{\rho}u_j'+\rho'\overline{u}_j+\rho'u_j'\\ e'\end{bmatrix},$$

$$(\boldsymbol{F}^{\nu})_i'=\begin{bmatrix}0\\ \tau_{ij}'\\ -\theta_i'+u_k'\overline{\tau}_{ki}+\overline{u}_k\tau_{ki}'\end{bmatrix},$$

$$\boldsymbol{F}_i'=\begin{bmatrix}\overline{\rho}u_i'+\rho'\overline{u}_i\\ \rho'\overline{u}_i\overline{u}_j+\overline{\rho}\,\overline{u}_iu_j'+\overline{\rho}u_i'\overline{u}_j+p'\delta_{ij}\\ u_i'(\overline{e}+\overline{p})+\overline{u}_i(e'+p')\end{bmatrix}+\begin{bmatrix}\rho'u_i'\\ \overline{\rho}u_i'u_j'+\rho'u_i'\overline{u}_j+\rho'\overline{u}_iu_j'+\rho'u_i'u_j'\\ u_i'(e'+p')\end{bmatrix}.$$

Neglecting density fluctuations and taking time averages of the NLDE causes the linear evolution terms and linear flux terms in the perturbations to vanish, which result in

$$\overline{\boldsymbol{LHS}}=\overline{\boldsymbol{RHS}}=\frac{\partial \boldsymbol{R}_i}{\partial x_i},$$

$$\boldsymbol{R}_i=\begin{bmatrix}0\\ \overline{\rho u_i'u_j'}\\ c_p\overline{\rho T'u_i'}+\overline{\rho}\,\overline{u_i'u_k'}\overline{u}_k+\frac{1}{2}\overline{\rho}\,\overline{u_i'u_i'u_k'}+\overline{u_k'\tau_{ki}}\end{bmatrix}. \tag{2}$$

The variables in formula (2) correspond to the standard Reynolds stress tensor and heat flux terms. These unknown terms need to be obtained in advance from a conventional, statistically steady-state RANS method.

2.2 FW–H acoustic analogy method

The penetrable integral solution of FW–H equation solved by Farassat et al. [30–35] can be written in the form of

$$\begin{aligned}4\pi p'(x_i,t)=&\iint\left[\frac{\dot{Q}_j\hat{n}_j}{r\,|1-M_r|^2}+\frac{Q_j\hat{n}_j(r\dot{M}_r+c_\infty(M_r-M^2))}{r^2\,|1-M_r|^3}\right]_{\rm ret}\mathrm{d}s\\ &+\iint\left[\frac{L_j\hat{r}_j(r\dot{M}_k\hat{r}_k+c_\infty(M_k\hat{r}_k-M^2))}{c_\infty r^2\,|1-M_r|^3}+\frac{L_j\hat{r}_j-L_jM_j}{r^2\,|1-M_r|^2}\right]_{\rm ret}\mathrm{d}s\\ &+\iint\left[\frac{\dot{L}_j\hat{r}_j}{c_\infty r\,|1-M_r|^2}+\frac{L_j\hat{r}_j-L_jM_j}{r^2\,|1-M_r|^2}\right]_{\rm ret}\mathrm{d}s+p_Q',\end{aligned} \tag{3}$$

where $Q_j=(\rho_\infty-\rho)v_j+\rho u_j$, $L_j=p\hat{n}_j+\rho u_j(u_i-v_i)n_i$, c_∞ and ρ_∞ are the speed of sound and density of undisturbed medium in the far-field; u_i and v_i denote the local velocities of flow medium and body surface respectively; $\hat{n}_i$ and $\hat{r}_i$ are the components of unit surface normal vector $\boldsymbol{n}$ and unit radiation vector $(\boldsymbol{x}-\boldsymbol{y})/r$; $r=|\boldsymbol{x}-\boldsymbol{y}|$ is the distance between observer and source positions in which $\boldsymbol{x}$ and $\boldsymbol{y}$ represent observer and source positions, respectively. The symbol $[\,]_{\rm ret}$ denotes evaluation at the retarded time $\tau=t-r/c_\infty$, τ and t are the observer and the source time, respectively; $M_r=v_i\hat{r}_i/c_\infty$ is the Mach number in the observer direction.

3 Validation of the method

To validate the method used in the present study, we have carried out broadband noise modeling for a benchmark problem, i.e., the flow past a circular cylinder of finite span, which has been extensively studied previously. The sketch of the problem is shown in Fig. 1a. The diameter of the rod is $d=10$ mm with span $l=30d$. We assume that the incoming airflow speed is $U_0=72$ m/s, corresponding to low Mach number $M=0.21$ in subcritical region as Reynolds number $Re_{\rm d}$ based on cylinder diameter is about 4.8×10^4. The vortex shedding frequency f_0 in the wake is about 1.4 kHz corresponding to Strouhal number $St=f_0d/U_0=0.20$.

According to the experiment [36], a spanwise correlation length is found as $2.7d$ in the cross flow past circular cylinder at $Re_{\rm d}=4.3\times10^4$. Here the spanwise correlation length in the flow past circular cylinder is chosen as $l_s=\pi d$

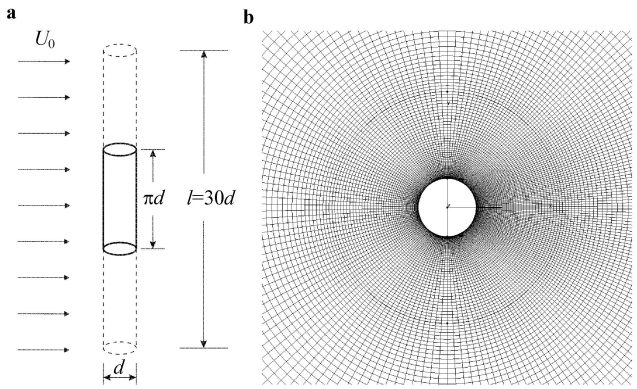

Fig. 1 Description of the benchmark problem. **a** Sketch of the flow past a circular cylinder. The diameter of the rod is $d = 10$ mm with span $l = 30d$; The incoming airflow speed is $U_0 = 72$ m/s; **b** O-type cylinderical grid distribution with about 10^6 mesh points: $31 \times 201 \times 151$ in the spanwise, circumferential and radial directions, respectively. The grid size of the first layer normal to the cylinder wall is $0.01d$

and the flow is assumed to be periodic in the spanwise direction. An O-type cylinderical grid (see Fig. 1b) is employed with about 10^6 mesh points: $31 \times 201 \times 151$ in the spanwise, circumferential and radial directions, respectively. The grid size of the first layer normal to the cylinder wall is $0.01d$ and the time step for NLAS computation is 2×10^{-5} s.

The variation of pressure coefficient on the circular cylinder is plotted in Fig. 2a. The calculation agrees well with the measurements of Batham [37]. Figure 2b shows the vorticity magnitude distribution on the cylinder, in which the maximum vorticity magnitude occurs at around 60° from the stagnation point.

The calculted sound pressure series at $r = 185d$ normal to the flow direction (90°) is shown in Fig. 3. As can be seen, the sound pressure changes periodically due to the vortex shedding in the flow past cylinder. The amplitude and period for sound pressure are 2 Pa and 7×10^{-4} s, corresponding to the vortex shedding frequency of around 1.4 kHz.

Far-field sound pressure level frequency spectra versus the Strouhal number at $r = 185d$ normal to the flow direction (90°) is compared with the experimental data in Fig. 4. Black

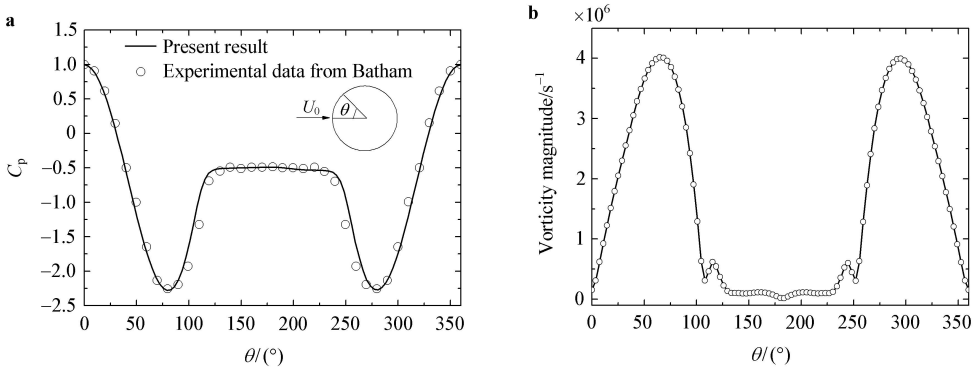

Fig. 2 Profiles of mean flow quantities on the circular cylinder. **a** Pressure coefficient, solid line represents the present result, hollow circles represents experimental data at $Re_d = 1.1 \times 10^5$ from Batham; **b** Vorticity magnitude, the maximum value occurs at around 60° from the stagnation point

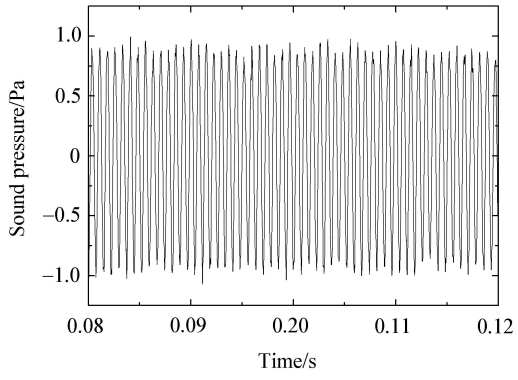

Fig. 3 Far-field sound pressure series at $r = 185d$ normal to the flow direction (90°). The amplitude and period for sound pressure are 2 Pa and 7×10^{-4} s, corresponding to vortex shedding frequency of around 1.4 kHz

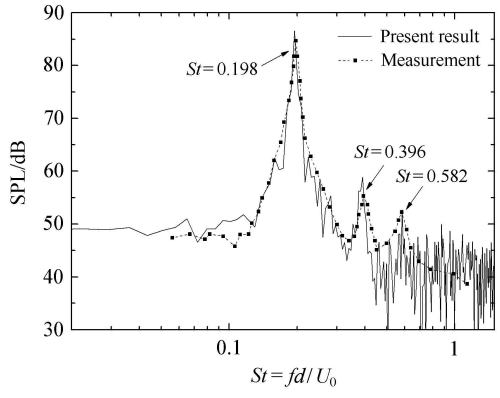

Fig. 4 Far-field sound pressure level frequency spectra at $r = 185d$ normal to the flow direction (90°); The acoustic peak corresponds to the shedding frequency of Karman vortex at $St = 0.198$, with other two minor peaks at $St = 0.396$ and 0.582

solid line represents the present simulated result while dashed line with solid squares is the measured data of Jacob et al. [38]. It is shown that the calculated sound pressure frequency spectra agree well with the experiment results. It is evident that the acoustic peak corresponds to the shedding frequency of Karman vortex at $St = 0.198$, with other two minor peaks at $St = 0.396$ and 0.582, all of which are in good agreements with the measurements. This test shows that the present hybrid computational methodology is qualitatively reasonable and quantitatively accurate.

4 Computational configurations

4.1 Physical model description

Our physical model is a simplified geometric structure of the real shape DSA350 high-speed pantograph system, as shown in Fig. 5. DSA350 pantograph is a single arm type pantograph in "Z" shape used on CRH2C and CRH380A high-speed trains in China. It consists of three electrical insulators supports, the base frame, articulated frame, panhead support and panhead. Two pantograph panheads on the top are current receptors contacting with power transmission line to transmit electricity from electrified wire net to the train. Panhead support is a structure which supports the panheads. The middle part with the shape of ">" is an articulated frame which provide suitable support force upward for the panheads so that they will contact well with the power transmission line and guarantee stable power supply for the train. The pantograph size is about $W = 1.5$ m, $L = 2.5$ m and $H = 1.5$ m in the x-, y- and z-directions, respectively. Figure 6 shows a schematic diagram of the computational domain. The pantograph is placed on the ground at the central position both in the x- and y-directions. The computational domain is $10W \times 20L \times 5H$ (in the x-, y-, z-directions, respectively). The boundaries are far enough from the pantograph so as to minimize the boundary effects on flow field around the computational model. The incoming flow is in the positive y-direction at a speed of 350 km/h.

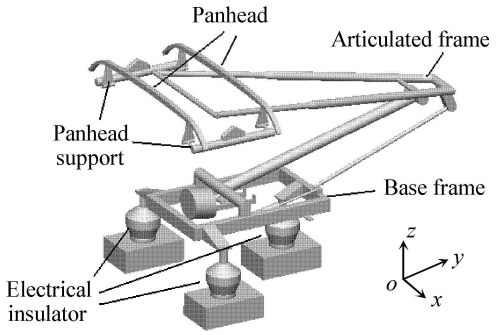

Fig. 5 Computational model of DSA350 high-speed pantograph system which is a single arm type pantograph used on CRH2C and CRH380A high-speed trains in China. The computational model has neglected some details of the real structures

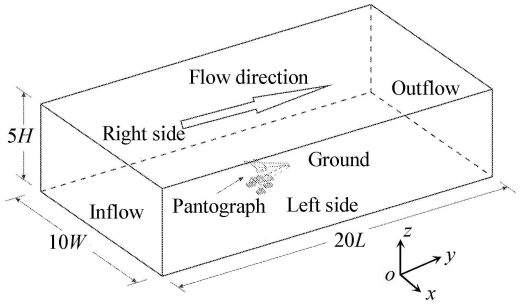

Fig. 6 Schematic diagram of the computational domain, the pantograph size is about $W = 1.5$ m, $L = 2.5$ m, $H = 1.5$ m in the x-, y- and z-directions, respectively. The computational domain is $10W \times 20L \times 5H$

To discretize the computational domain, a hybrid grid blended with unstructured tetrahedrons and triangular prisms was created with a total number of grid cells of around 9.6 million. In order to take into account more appropriately the effects of boudary layers, five layers of triangular prims are set on the surface of the pantograph with a total height of 10 mm and a ratio of 1.2 between two adjacent layers. The grid size on the surface of the pantograph is not larger than 10 mm. The triangular prisms are connected with unstructured tetrahedrons. The mesh is further refined around and downstream the pantograph so as to simulate the flow field more accurately (see Fig. 7).

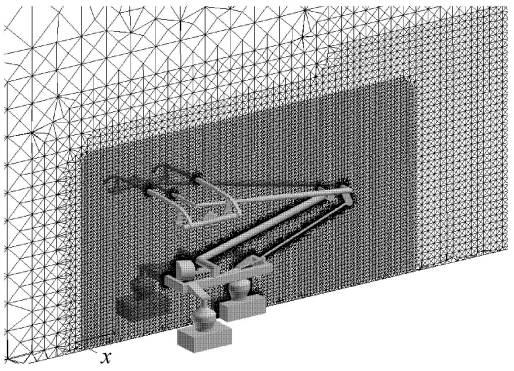

Fig. 7 Schematic of grid distribution around the computational model. A hybrid grid blended with unstructured tetrahedrons and triangular prisms was created with a total number of grid cells of around 9.6 million. Five layers of triangular prims are set on the surface of the pantograph with a total height of 10 mm and a ratio of 1.2 between two adjacent layers. The grid size on the surface of the pantograph is not larger than 10 mm

4.2 Computational conditions

For air in standard state, the necessary parameters are selected as $\rho_\infty = 1.25\,\mathrm{kg/m^3}$, $p_\infty = 0.1$ MPa, $T_\infty = 288$ K and

$\mu_\infty = 17.16\,\mathrm{mg/(m{\cdot}s)}$. In the stage of quasi-steady RANS computation, boundary conditions are set up as follows: non-slip condition is applied at the ground and solid surface of the pantograph system; at the front of the computational domain is the incoming flow condition of $U_\infty = 350\,\mathrm{km/h}$, the pressure gradient along the flow direction vanishes at the rear exit; the other three far-field boundaries are characteristic boundary conditions with characteristic speed of 350 km/h. In the stage of aerodynamic noise simulation of NLAS, for the ground and solid surface of the pantograph system non-slip condition is adopted, while for the rest NLAS outer boundary conditions are adopted. Except for the ground and pantograph surface we assume all the others are non-reflecting boundaries with far-field absorbing layers to avoid pollution of the sound wave reflection in the acoustic field.

The computational time-step size for NLAS is 20 μs, corresponding to the maximum frequency range of 25 kHz in aerodynamic noise calculation. When the flow was statistically steady, 5 000 steps were performed to store the flow data on acoustic control surface to acquire a total flow time of 0.1 s. The resolution of aerodynamic noise in frequency domain is around 5 Hz.

5 Results and discussions

The numerical simulations were carried out on a Linux parallel computation platform with 64 CPUs. It took about 50 h to finish RANS calculation for a quasi-steady initial flow field and about 135 h for the time-dependent NLAS computation (7 500 time steps with about 65 s per time step). The total computational time was about 12 000 CPU-hours.

5.1 Flow field results

5.1.1 Orders of magnitude analysis for principal noise sources

In the light of aeroacoustics theory, there are three principal sources for flow noise: mass or momentum flux as monopole sources, surface forces (surface fluctuating pressure p' and wall shear stress τ) as dipole, Lighthill stress tensor $T_{ij} = \rho_0 u_i u_j$ as quadrupole. There is no mass or momentum flux in the present case and we will compare the other three sources. The Lighthill quadrupole source term $\rho_0 \dfrac{\partial^2 u_i u_j}{\partial x_i \partial x_j}$ is equivalent to the term $\rho_0 \nabla \cdot (\boldsymbol{\omega} \times \boldsymbol{u})$ on the right side of Powell's vortex sound equation [39] for incompressible isentropic flow at low Mach numbers

$$\left(\frac{1}{c_0^2}\frac{\partial^2}{\partial t^2} - \nabla^2\right) p_\mathrm{a} = \rho_0 \nabla \cdot (\boldsymbol{\omega} \times \boldsymbol{u}), \tag{4}$$

where c_0 is sound speed, p_a denotes far-field acoustic pressure, $\boldsymbol{u}$ and $\boldsymbol{\omega}$ are velocity and vorticity in the flow field. By dimensional analysis, we have the orders of magnitude for acoustic pressure related to vortices

$$p_\mathrm{a} \propto \rho_0 U^2. \tag{5}$$

Figure 8 shows instantaneous contours of surface fluctuating pressure and wall shear stress on the surface of pantograph. The magnitude of surface fluctuating pressure and wall shear stress are of the orders of 10^4 and 10^1, respectively. Therefore, the orders of magnitude for acoustic pressure generated by three sources are

$$10^4 : 10^1 : \rho_0 U^2 = 10^4 : 10^1 : 10^4. \tag{6}$$

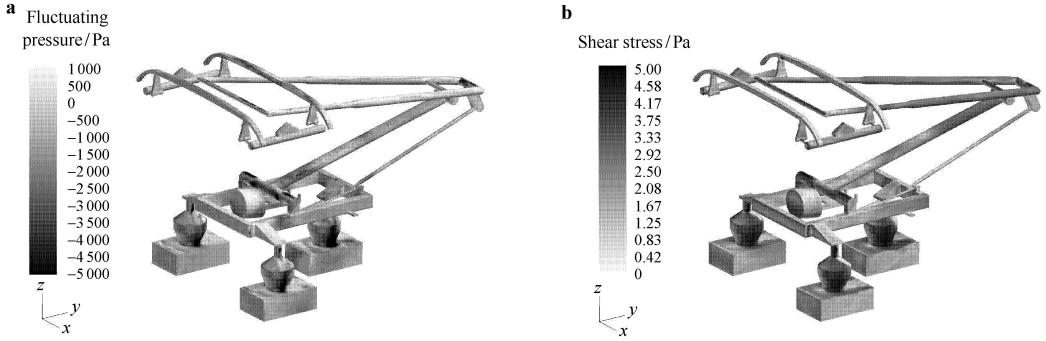

Fig. 8 Instantaneous contours of flow variables on the surface of pantograph. **a** Surface fluctuating pressure; **b** Wall shear stress

Based on the above analysis, the contributions of wall shear stress is far less important than the other two sources in the present study. However, surface fluctuating pressure and vortices are equally important for far-field noise prediction.

5.1.2 Contours of vortices on the longitudinal y-z plane

According to Powell's vortex sound theory [39], vortex is a significant source in the production of flow sound, that is, the term $\nabla \cdot (\boldsymbol{\omega} \times \boldsymbol{u})$ on the right hand side of the equation is the sound source term. Figure 9 shows transient contours of vortices on three *y*-*z* planes at $x = -0.55\,\mathrm{m}$, $x = 0\,\mathrm{m}$ and $x = 0.55\,\mathrm{m}$ respectively. The flow is disturbed by various components of the pantograph. Periodic vortex shedding from structures such as pantograph panheads and base frame can be seen clearly. Vortices produced by the front panhead hit the surface of the rear panhead and generate fluctuating

force. The interactions between vortices of these two components are also very complex. Large flow separation and complicated wake flow appear downstream.

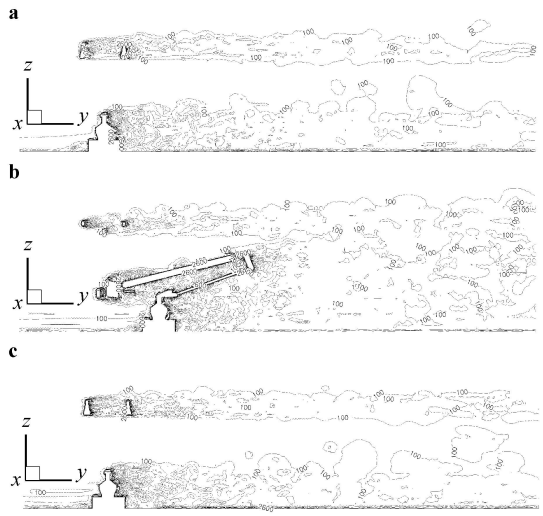

Fig. 9 Transient contours of vortices on three *y*-*z* planes. **a** $x = -0.55$ m; **b** $x = 0$ m; **c** $x = 0.55$ m. The flow is in the positive *y*-direction and the typical vorticity magnitude is between 100 and 2 600

5.1.3 Flow structure in the wake of pantograph

Transient iso-surfaces of vorticity of different orders of magnitude are displayed in Fig. 10, demonstrating where and how strong and weak eddies are distributed. Coherent structures of large vortexes stem from the leading surface of panheads or base frame, develop in the wake of pantograph, break up into small ones and finally impact on surrounding fluids or other solid surface, which generate strong pressure fluctuations that radiate flow noises.

5.2 Near-field fluctuating pressure and vorticity fields

By time-dependent calculation of NLAS, the near-field acoustic result can be obtained. Acoustic pressure is defined as pressure fluctuation, namely, the difference between instantaneous pressure and the averaged one. The instantaneous acoustic pressure distribution in the vertical central section of $x = 0$ plane in Fig. 11 shows that acoustic waves are generated from panheads and base frame and then radiate outwards. The periodic vortex shedding from these structural components radiates sound at the same time. Therefore, panheads and base frame are the most important sources of noise. They should be shaped in streamlined bodies for noise reduction.

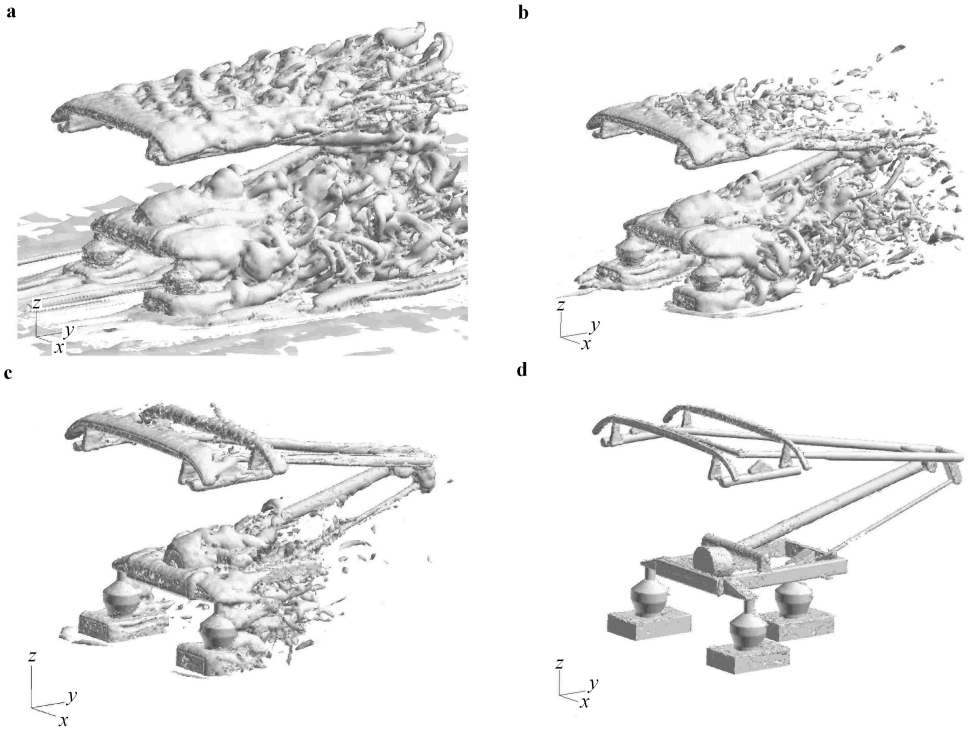

Fig. 10 Transient iso-surfaces of vorticity of different orders of magnitude of **a** 5×10^2, **b** 10^3, **c** 2×10^3 and **d** 10^4, respectively

Moreover, aerodynamic noises of the pantograph system are caused by the unsteady wake flow or the flow separation disturbed by a variety of components/structures and the complicated interactions between them. Some components generate broadband noises while most of them create aeolian tones which can be identified by the peaks in frequency

spectra. The genesis mechanism of this noise is characterized by periodic vortex shedding. When vortices shed from the surface of slender components, they impact on the surrounding fluid or solid surface and generate fluctuating force which results in strong pressure fluctuation. The generated force also fluctuates with the same frequency as the vortex shedding. A fluctuating force creates dipole sound.

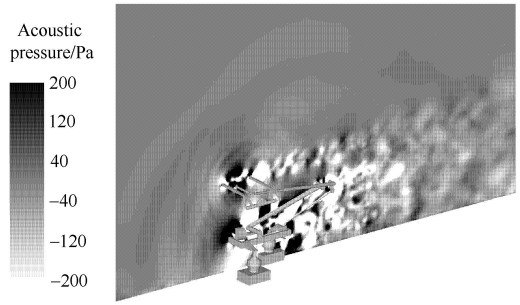

Fig. 11 Instantaneous acoustic pressure distribution in the vertical central section of $x = 0$ plane. The dark and light colors represent positive and negative values, respectively

5.3 Far acoustic field

Time series of instantaneous acoustic pressure at any observer point in the far-field is acquired by the integrals of FW–H formulation over the penetrable integral control surface. By the use of fast Fourier transformation (FFT), sound pressure level and frequency spectra characteristics are obtained. The magnitude of acoustic level is presented in terms of sound pressure level (SPL) in the decibel scale (dB), defined as

$$L_{\mathrm{p}} = 20 \lg \frac{p_{\mathrm{e}}}{p_{\mathrm{ref}}}, \tag{7}$$

where p_{e} is the effective sound pressure corresponding to root-mean squared sound pressure; p_{ref} denotes a reference pressure taken as the value of threshold of human audibility in air, $p_{\mathrm{ref}} = 2 \times 10^{-5}\,\mathrm{Pa} = 20\,\mu\mathrm{Pa}$. For sound frequency spectra, SPL values are plotted against their corresponding frequency. Using the sound frequency spectra, the overall sound pressure level (OASPL) can be calculated by summing up all the acoustic energy in the whole frequency domain, which is expressed in the form of

$$L_{\mathrm{pZ}} = 10 \lg \sum_i 10^{L_{\mathrm{pi}}/10}. \tag{8}$$

If A-weighting filter is used, SPL will be given in terms of dB(A) that we call A-weighted SPL, which is denoted by L_{AP}. A-weighted SPL, widely used in acoustic measurements, can better reflect the actual feeling of sound loudness for human being.

5.3.1 Frequency spectra characteristics of SPL at a standard observer point

According to the standards of ISO 3095-2005, the standard observer points should be 25 m from the central line of rail track and 3.5 m above the surface of rail track. Here we choose (25 m, −8.0 m, 3.5 m) as the coordinate of standard observer point. A-weighted SPL is employed to evaluate the noise level according to international standards.

Figure 12 shows one-third octave band frequency spectra of aerodynamic noise at the standard observer point. As can be clearly demonstrated by the figure, aerodynamic noise radiated by the pantograph is a typical broadband noise whose frequency spectra cover a wide range of frequency from 20 Hz to above 20 kHz. However, most of the acoustic power is restricted in the medium-high frequency range from about 200 Hz to 5 kHz.

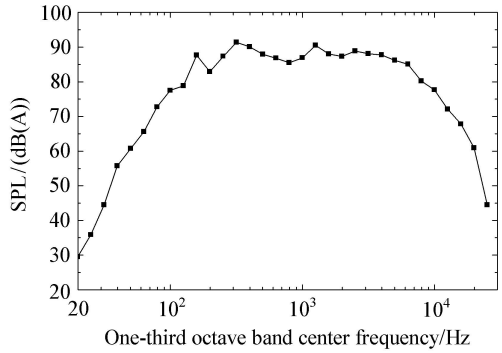

Fig. 12 One third octave band frequency spectra of aerodynamic noise at the standard observer point (25 m from the central line of rail track and 3.5 m above the surface of rail track)

5.3.2 Acoustic attenuation with respect to distance

Five observer points are spanwisely selected at 6.25 m, 12.5 m, 25 m, 50 m and 100 m away from the central plane $x = 0$, respectively. The distances between adjacent ones are doubled. Their coordinates are listed in Table 1.

Table 1 The coordinates of each observer site

Observer sites	1	2	3	4	5
x-coordinate/m	6.25	12.5	25	50	100
y-coordinate/m	−8.0	−8.0	−8.0	−8.0	−8.0
z-coordinate/m	3.5	3.5	3.5	3.5	3.5

Acoustic attenuation characteristics are displayed in Fig. 13 where the OASPL at each site is plotted versus their respective distance to the central plane $x = 0$ of pantograph system. It can be seen from the figure that with the distance doubled, the magnitude of acoustic attenuation magnitude vary from 5.06, 5.70 to 5.99 decibel, respectively. That is, the magnitude of acoustic attenuation approximates to 6 decibel when the observation site is far from 25 m. As we know, SPL of spherical wave drops by 6 dB with the doubling of distance while for cylindrical wave, this value is only 3 dB. The observation implies that like a point source, aerodynamic noise of the pantograph system radiates outwards approximately in the form of spherical wave in the distance.

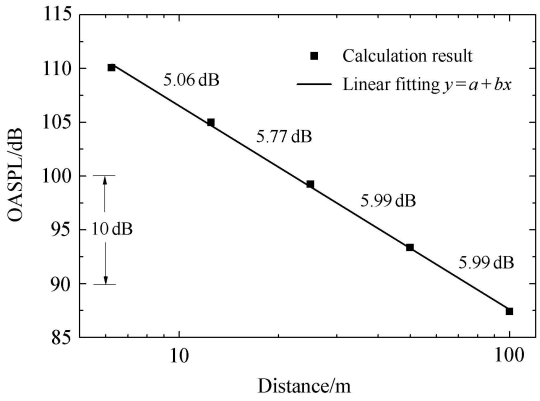

Name	Description
Equation	$y=a+bx$
Weight	No weighting

Parameters	Value
Intercept value	110.401 77
Intercept standard error	0.242 54
Slope value	−18.932 24
Slope standard error	0.328 92
Statistics adj. R-square	0.998 79

Fig. 13 Acoustic attenuation with respect to distance from the pantograph system, the numbers above the solid line denote decreasing magnitude between adjacent observer points

5.3.3 Aerodynamic noise with respect to different speed levels

Previous studies have demonstrated that the train speed may enormously influence the aerodynamic noise. In this section, we would examine the variation of aerodynamic noise of pantograph system versus train speed. And so case studies were performed for 200 km/h, 250 km/h, 300 km/h, 350 km/h, 400 km/h, 450 km/h and 500 km/h, respectively.

Figure 14 is the OASPL along $x = 25$ m, $z = 3.5$ m at different speed levels, showing that OASPL grows remarkably with the speed. From the difference of OASPL among various speeds, it is found that it increases almost logarithmically with the speed. The central position of the pantograph system is located at $y = -8$ m of dashed line A. The maximum OASPL is located not at position A but at B which is several meters downstream of the pantograph. From this phenomenon we can further confirm our previous conclusion that the aerodynamic noise of pantograph system is generated by the unsteady wake flow disturbed by various structural components and the complicated interactions between them.

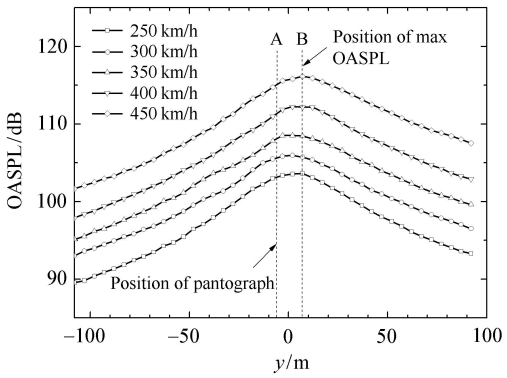

Fig. 14 OASPL along $x = 25$ m, $z = 3.5$ m at different speed levels. The flow is in the positive y-direction. The pantograph is located at $y = -8$ m denoted by dashed line A. Dashed line B is the position of maximum OASPL

The variation of OASPL versus speed at standard observer point is displayed in Fig. 15. The solid squares are calculated values while the solid line is logarithm fitting of these data, written in terms of equation as

$$L_{\mathrm{pZ}} = 40.61 \lg \frac{U}{U_0} + L_{\mathrm{pZ0}}, \tag{9}$$

where L_{pZ0} is the OASPL value at speed U_0. Compared with the definition $L_{\mathrm{p}} = 20 \lg(p/p_{\mathrm{ref}}) = 10 \lg(W/W_{\mathrm{ref}})$, in which W and W_{ref} are the acoustic power and reference acoustic power, we can find that the acoustic power of pantograph system is approximately proportional to the 4th power of speed. In figure 12 of Ref. [12], Wakabayashi et al. gave aerodynamic noise radiated by pantograph system of FASTECH360Z and FASTECH360S with respect to train speed using microphone array. They can be expressed in the same logarithm form of Eq. (9)

$$L_{\mathrm{pZ}} = a \lg \frac{U}{U_0} + L_{\mathrm{pZ0}}. \tag{10}$$

The slopes a were 60.46, 51.06, 42.47 and 43.11 for the four cases, respectively. Therefore, pantograph noises of FASTECH360Z and FASTECH360S approximately grow as power law of speed to the order between 4th and 6th. Our computational result is in accordance with the field measurements for pantograph of FASTECH360S.

5.3.4 Effects of pantograph cover on aerodynamic noise

It has been demonstrated that by installation of pantograph cover on high-speed trains, aerodynamic noise of pantograph can be reduced considerably. Pantograph cover is generally composed of a front spoiler, a rear spoiler and a pair of baffles on both sides. The front spoiler of the cover reduces the speed of incoming flow and the baffles on both sides play the role of noise barriers. However, the cover itself may generate aerodynamic noise at the same time. The most suitable configuration and composition of cover and pantograph have to be determined by careful analysis and comparison.

To consider noise reduction effects of pantograph cover

on aerodynamic noise, four types of pantograph covers are studied in this section. Figure 16 shows the configuration of pantograph covers. It consists of a pair of baffles with half of the height of the pantograph on both sides in Case 1. For Case 2, the pantograph cover is closed up all around. The front spoiler of the cover is moved forward and separated by an inter-coach spacing in Case 3. The cover in Case 4 consists of a front spoiler, a pair of baffles and a rear spoiler.

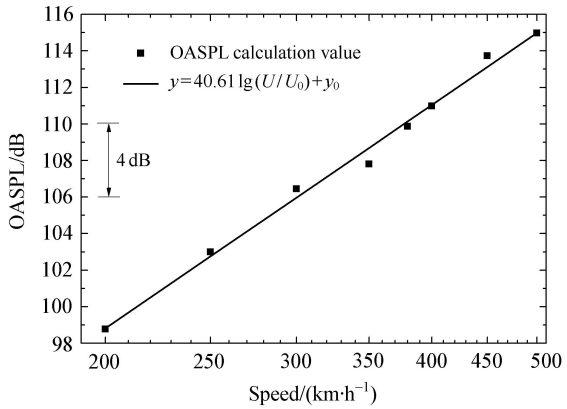

Name	Description
Equation	$y=a+bx$
Weight	No weighting

Parameters	Value
Intercept value	98.8236
Intercept standard error	0.37391
Slope value	40.6076
Slope standard error	1.4258

Fig. 15 Variation of OASPL versus speed at standard observer point. The horizontal axis is in logarithm coordinates to the base 10. The solid squares are calculation values and the solid line is logarithm fitting of these data

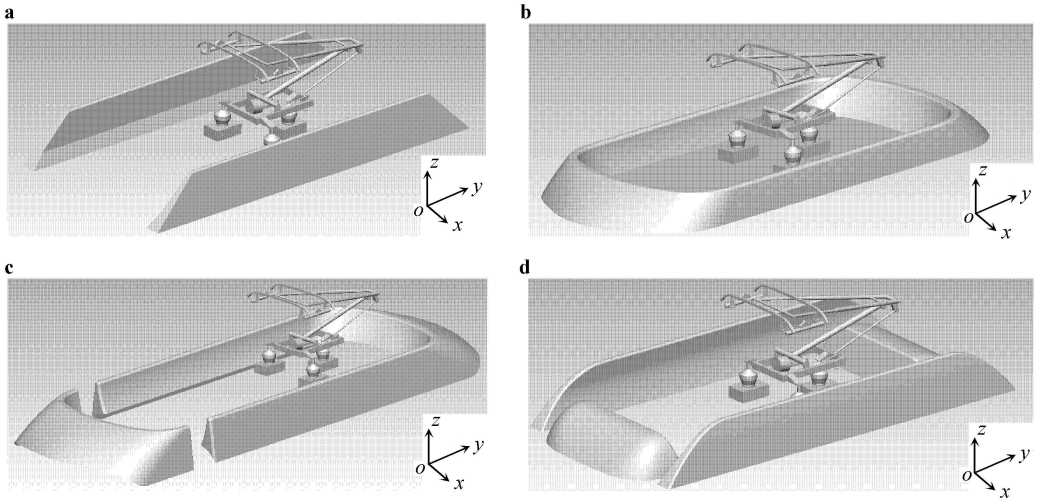

Fig. 16 Four cases with different types of pantograph covers. **a** Case 1, a pair of baffles with half of the height of the pantograph on both sides; **b** Case 2, closed up all around; **c** Case 3 with the front spoiler of the cover moved forward and separated by an inter-coach spacing; **d** Case 4, a front spoiler, a pair of baffles and a rear spoiler

OASPLs for different cases are plotted in Fig. 17. The solid line represents the case without pantograph cover. The computational results imply that among the four covers only Case 1 can lessen the total noise by about 3 dB. Noise levels of the other three cases are all higher than that of the original case. The baffles on both sides in Case 1 are noise barriers which partially shield the propagation of sound wave in the spanwise direction. The baffle is streamline-shaped and the projected area in the flow direction is very small. These factors can help to reduce flow disturbances caused by the cover, and thus generate less aerodynamic noise itself. OASPL of Case 2 is the highest among the four cases. Figure 18 shows instantaneous velocity disturbance magnitude of Case 2 in the vertical central section of $x = 0$ plane. Although the front and rear edges of this cover can reduce the flow velocity past the base frame and thus decrease pantograph noise, they might produce additional cavity noise themselves as a typical cavity flow is formed in the cover. Aerodynamic noise generated by the cover itself lead to the rise of total noise so that OASPLs of Case 2 to Case 4 are higher than that of the original case. Based on this sort of mechanism analysis, pantograph cover consisting of a pair of baffles on both sides is suggested to install on trains as a countermeasure for aerodynamic noise reduction.

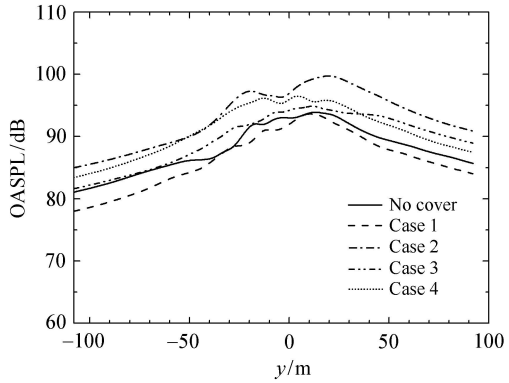

Fig. 17 OASPL along $x = 25$ m, $z = 3.5$ m for different cases. The solid line represents the case without pantograph cover, the dash line is Case 1, the dash-dot line is Case 2, the dash-dot-dot line is Case 3, and the short dot line is Case 4

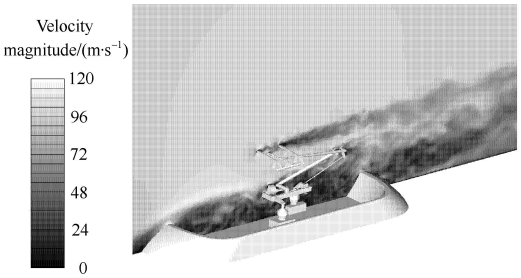

Fig. 18 Instantaneous velocity magnitude distribution of Case 2 in the vertical central section of $x = 0$ plane

6 Conclusions

In this study, a hybrid NLAS/FW–H method validated by a benchmark problem of flow around a circular cylinder of finite span is utilized to investigate the characteristics of aerodynamic noise of high-speed train pantograph systems. Based on the computation results and mechanism analysis, the following conclusions can be drawn:

(1) Aeroacoustic noise of pantograph system is generally caused by the unsteady wake flow or flow separation disturbed by a variety of components/structures and the complicated interactions between them. Some components generate broadband noise while most of them create aeolian tones. The periodic vortex shedding from slender components is the principal genesis mechanism. The complicated interaction between shedding vortices from different structural components needs further investigation;

(2) The frequency spectra characteristics are analyzed, showing that the aerodynamic noise of pantograph system is a typical broadband noise which covers a wide range of frequency. However, most acoustic power is restricted in the medium-high frequency range from about 200 Hz to 5 kHz. And the diameters of rod components from several millimeters to about 10 cm happen to correspond to vortex shedding frequency in the same range, which is strongly dependent on the shedding of vortex from various components;

(3) Acoustic attenuation with respect to observation distance are also examined, and the results show that the aerodynamic noise radiated by the pantograph system radiates outwards approximately in the form of spherical wave in the far field farther than 25 m. In contrast, the acoustic noise in the near field behaves like something between spherical and cylindrical waves;

(4) The calculation of OASPL at different speed levels demonstrates that it grows logarithmically with respect to the train speed. Accordingly, the acoustic power approximately grows as the 4th power of speed;

(5) Noise reduction effects of four types of pantograph covers are estimated and compared. The computations indicate that among the four cases only the cover of type 1 can lessen noise by about 3 dB because the baffles on both sides play the role of noise barriers. Although the front and rear edges of the other three cases can reduce the flow speed past the base frame and thus decrease pantograph noise, they might produce additional cavity noise themselves. Pantograph cover composed of a pair of baffles on both sides is suggested to install on trains to lessen flow noise of the pantograph system.

Acknowledgements The authors appreciate An Yi, Zhang Zi-Bing for their valuable assistance in the computation. Both "Computing Facility for Computational Mechanics, Institute of Mechanics, Chinese Academy of Sciences" and "Supercomputing center of Chinese Academy of Sciences" are gratefully acknowledged. Finally, we would like to thank the reviewers for their valuable comments and suggestions.

References

1 Talotte, C., Gautier, P.E., Thompson, D.J., et al.: Identification, modeling and reduction potential of railway noise sources: A critical survey. Journal of Sound and Vibration **267**, 447–468 (2003)

2 Ikeda, M.: The development of low noise pantograph. Foreign Locomotive and Rolling Stock Technology **5**, 30–31 (1995) (in Chinese)

3 Zhang, S.G.: Noise mechanism, sound source localization and noise control of 350 km·h^{-1} high-speed train. China Railway Science **30**, 86–90 (2009) (in Chinese)

4 Noger, C., Patrat, J.C., Peube, J., et al.: Aeroacoustical study of the TGV pantograph recess. Journal of Sound and Vibration **231**, 563–575 (2000)

5 Takaishi, T., Ikeda, M., Kato, C.: Effects of periodic holes on the suppression of aeroacoustic noise from a pantograph horn. In: Proceedings of ASME FEDSM'03 4th ASME/JSME Joint Fluids Engineering Conference. Hawaii, USA, July 6-10 (2003)

6 Shibata, K., Hirai, M., Hariyama, T., et al.: Development of low noise pantograph adopted to the superexpress HAYATE. Mitsubishi Heavy Industries Technical Review **40**, 154–157 (2003)

7 Nagakura, K.: Localization of aerodynamic noise sources of Shinkansen trains. Journal of Sound and Vibration **293**, 547–556 (2006)

8 Murata, K., Sato, T., Sasaki, K.: Countermeasures of noise reduction for Shinkansen electric-current collecting system and lower parts of cars. JR EAST Technical Review **1**, 13–21 (2002)

9 Kurita, T., Hara, M., Horiuchi, M.: Reduction of pantograph noise. JR EAST Technical Review **8**, 19–22 (2006)

10 Kurita, T., Hara, M., Yamada, H., et al.: Reduction of pantograph noise of high-speed trains. Journal of Mechanical Systems for Transportation and Logistics **3**, 63–74 (2010)

11 Yamada, H., Wakabayashi, Y., Kurita, T., et al.: Noise evaluation of Shinkansen high-speed test train (FASTECH360S, Z). In: Proceedings of the 8th World Congress on Railway Research. Seoul, Korea, May 18-22 (2008)

12 Wakabayashi, Y., Kurita, T., Yamada, H., et al.: Noise measurement results of Shinkansen high-speed test train (FASTECH360S, Z). In: Schulte-Werning, B., et al. eds. Noise and Vibration Mitigation for Rail Transportation Systems, Notes on Numerical Fluid Mechanics and Multidisciplinary Design. Springer, Berlin Heidelberg, New York **99**, 63–70 (2008)

13 Yamazaki, N., Takaishi, T., Toyooka, M., et al.: Wind tunnel tests on the control of aeroacoustic noise from high speed train. In: Schulte-Werning, B., et al. eds. Noise and Vibration Mitigation for Rail Transportation Systems, Notes on Numerical Fluid Mechanics and Multidisciplinary Design. Springer, Berlin Heidelberg, New York **99**, 33–39 (2008)

14 Wakabayashi, Y., Kurita, T., Horiuchi, M.: Development of pantograph noise insulating panels. JR EAST Technical Review **12**, 28–33 (2008)

15 Sueki, T., Ikeda, M., Takaishi, T.: The aerodynamic noise reduction by porous materials and application to a current collector. RTRI Report **22**, 11–16 (2008)

16 Ikeda, M.: The latest noise reduction technology in pantographs. Railway Research Review **66**, 18–21 (2009)

17 Ikeda, M., Mitsumoji, T., Sueki, T., et al.: Aerodynamic noise reduction of a pantograph by shape-smoothing of panhead and its support and by the surface covering with porous material. In: Maeda, T., et al. eds. Noise and Vibration Mitigation for Rail Transportation Systems, Notes on Numerical Fluid Mechanics and Multidisciplinary Design. Springer, Berlin Heidelberg, New York **118**, 419–426 (2012)

18 Talotte, C.: Aerodynamic noise: A critical survey. Journal of Sound and Vibration **231**, 549–562 (2000)

19 Holmes, B.S., Dias, J.B., Jaroux, B.A., et al.: Predicting the wind noise from the pantograph cover of a train. International Journal for Numerical Methods in Fluids **24**, 1307–1319 (1997)

20 Kitagawa, T., Nagakura, K.: Aerodynamic noise generated by Shinkansen cars. Journal of Sound and Vibration **231**, 913–924 (2000)

21 Sassa, T., Sato, T., Yatsui, S.: Numerical analysis of aerodynamic noise radiation from a high-speed train surface. Journal of Sound and Vibration **247**, 407–416 (2001)

22 Yang, F., Zheng, B.L., He, P.F.: Numerical simulation on aerodynamic noise of power collection equipment for high-speed trains. Computer Aided Engineering **19**, 44–47 (2010) (in Chinese)

23 Masson, E., Paradot N., Allain, E.: The numerical prediction of the aerodynamic noise of the TGV POS high-speed train power car. In: Maeda, T., et al. eds. Noise and Vibration Mitigation for Rail Transportation Systems, Notes on Numerical Fluid Mechanics and Multidisciplinary Design. Springer, Berlin Heidelberg, New York **118**, 437–444 (2012)

24 Jiang, M., Li, X.D., Bai, B.H., et al.: Numerical simulation on the NACA0018 airfoil self-noise generation. Theoretical & Applied Mechanics Letters **2**, 052004 (2012)

25 Lighthill, M.J.: On sound generated aerodynamically. I. General theory. Philosophical Transactions of the Royal Society of London. Series A **211**, 564–587 (1952)

26 Bailly, C., Juve, D.: Numerical solutions of acoustic propagation problems using linearized Euler equations. AIAA Journal **38**, 22–29 (2000)

27 Batten, P., Ribaldone, E., Casella, M., et al.: Towards a generalized non-linear acoustics solver. AIAA-2004-3001, 10th AIAA/CEAS Aeroacoustics Conference. Manchester, United Kingdom, May 10-12 (2004)

28 Goldberg, U., Peroomian, O., Palaniswamy, S., et al.: Anisotropic k-epsilon model for adverse pressure gradient flow. AIAA paper 99-0152, 37th AIAA Aerospace Sciences Meeting and Exhibit. Reno, United States, January 11-14 (1999)

29 Ffowcs Williams, J.E., Hawkings, D.L.: Sound generation by turbulence and surfaces in arbitrary motion. Philosophical Transactions of the Royal Society of London. Series A **264**, 321–342 (1969)

30 Farassat, F.: Theory of noise generation from moving bodies with an application to helicopter rotors. NASA Technical Report R-451 (1975)

31 Farassat, F.: Linear acoustic formulas for calculation of rotating blade noise. AIAA Journal **19**, 1122–1130 (1981)

32 Farassat, F., Succi, G.P.: A review of propeller discrete frequency noise prediction technology with emphasis on two current methods for time domain calculations. Journal of Sound and Vibration **71**, 399–419 (1980)

33 Farassat, F.: Introduction to generalized functions with applications in aerodynamics and aeroacoustics. NASA Technical Paper 3428 (1996)

34 Farassat, F.: The Kirchhoff formulas for moving surfaces in aeroacoustics-the subsonic and supersonic cases. NASA Technical Memorandum 110285 (1996)

35 Farassat, F.: Derivation of formulations 1 and 1A of Farassat. NASA/TM-2007-214853 (2007)

36 Szepessy, S.: On the spanwise correlation of vortex shedding from a circular cylinder at high subcritical Reynolds number. Physics of Fluids **6**, 2406–2416 (1994)

37 Batham, J.P.: Pressure distributions on circular cylinders at critical Reynolds number. Journal of Fluid Mechanics **57**, 209–228 (1973)

38 Jacob, M.C., Boudet, J., Casalino, D., et al.: A rod-airfoil experiments as a benchmark for broadband noise modeling. Theoretical and Computational Fluid Dynamics **19**, 171–196 (2005)

39 Powell A.: Theory of vortex sound. Journal of Acoustical Society of America **36**, 177–195 (1964)